Calibration Strategy of the JUNO Experiment

JUNO collaboration[1]

[1] School of Physics and Astronomy, Shanghai Jiao Tong University, Shanghai Key Laboratory for Particle Physics and Cosmology, Shanghai, 200240, China

Abstract: We present the calibration strategy for the 20 kton liquid scintillator central detector of the Jiangmen Underground Neutrino Observatory. By utilizing a comprehensive multiple-source, multiple-position calibration program, in combination with a dual calorimetry approach with two independent sets of photosensors, we demonstrate that the JUNO central detector can achieve a better than 1% linear energy scale and a superior effective energy resolution of 3%, required by the neutrino mass hierarchy determination.

Key words: JUNO, Neutrino mass hierarchy, Calibration, Radioactive sources, Double calorimetry

1 Introduction

The massive nature of neutrinos have been firmly established by the neutrino oscillation experiments [1, 2], but the ordering of the three mass eigenstates, m_1, m_2, and m_3, remains unclear. The solar neutrino experiment has established that $m_2 > m_1$. The gap between m_3 and (m_1, m_2) is significantly larger, but experimentally there has been no clear evidence whether m_3 is the largest or smallest. This is the so-called neutrino mass hierarchy (MH) problem.

The Jiangmen Underground Neutrino Observatory (JUNO) is a multi-purpose experiment to elucidate fundamental neutrino properties as well as to study neutrinos with astrophysical or terrestrial origins [3]. Its central detector (CD) is a 20-kton liquid scintillator (LS) detector, located 700 m underground in Guangdong, China. The detector is at an equal distance of 53 km from the Yangjiang and Taishan nuclear power plants along the south China coast. Such a median baseline configuration is ideal for the determination of neutrino MH using the electron anti-neutrinos from the reactors [4–7]. Due to neutrino oscillation, the survival probability of anti-electron neutrinos can be written as:

$$P_{\overline{\nu_e} \to \overline{\nu_e}} = 1 - \sin^2 2\theta_{13} \times$$
$$\left(\cos^2 \theta_{12} \sin^2(\Delta m_{31}^2 \frac{L}{4E^\nu}) + \sin^2 \theta_{12} \sin^2(\Delta m_{32}^2 \frac{L}{4E^\nu}) \right) \quad (1)$$
$$- \cos^4 \theta_{13} \sin^2 2\theta_{12} \sin^2(\Delta m_{21}^2 \frac{L}{4E^\nu})$$

In this expression, θ_{12} and θ_{13} are the neutrino mixing angles, $\Delta m_{ij}^2 \equiv m_i^2 - m_j^2$ is the mass-square-difference between eigenstates i and j, L is the distance from neutrino production to detection (baseline), and E^ν is the energy of the neutrino. Numerically, $|\Delta m_{32}^2|$ and $|\Delta m_{31}^2|$ are mostly degenerate ($\sim 2.5 \times 10^{-3}$ eV^2), and Δm_{21}^2 is much

less with a value $\sim 7.5 \times 10^{-5}$ eV^2. For the so-called normal or inverted hierarchy, $|\Delta m_{31}^2| = |\Delta m_{32}^2| \pm \Delta m_{21}^2$. Due to the fact that $\theta_{12} \sim 30°$, the two oscillation frequencies driven by Δm_{31}^2 and Δm_{32}^2 are weighted differently in Eqn. 1 and the main information of mass hierarchy come from a region with neutrino energy between 3 and 6 MeV, which allows one to determine the hierarchy if the oscillation pattern in E_ν can be measured with unprecedented high precision.

The JUNO LS is contained inside a 35-m diameter acrylic sphere with 12 cm thickness, strengthened by 591 stainless steel (SS) connection bars. About 18,000 20-inch and 25,000 3-inch photomultipliers (PMTs) are closely packed and immersed in ultra-pure water outside the sphere viewing the LS. These two sets of photosensors and their corresponding readout electronics, constitute the LPMT (large) and the SPMT (small) systems. The SPMT was introduced to enable a redundant calorimetry metric called "dual calorimetry". This technique, implemented in JUNO for the first time, exploits the complementary differences between of both readout systems to yield unique response insight. The electron anti-neutrinos are detected via the so-called inverse β-decay (IBD), $\bar{\nu}_e + p \to e^+ + n$, where the electron anti-neutrinos interact with protons in the LS then produce positrons and neutrons. The positron will deposit its kinetic energy promptly with a range between 0 to 8 MeV in the LS, then annihilate with an electron producing gamma rays. The energy of the anti-neutrino is related to the kinetic energy of the positron as $E^\nu \approx E^{e^+} + 1.8$ MeV. The neutron will be captured on a proton within about 200 μs, producing a delayed 2.22 MeV gamma.

Particle interactions in the LS will produce scintillating (dominating) and Cerenkov (sub-dominant) photons, which will be converted to photoelectrons (PE) by the PMTs and read out by electronics. Let us now consider

---

the nonlinearity of the energy scale intrinsic to the LS. The scintillation photons has a known Birks' "quenching" effect [1], and the Cerenkov emission depends on the velocity of the charged particle. The combined effect is clearly both energy and particle dependent, and will be referred to as the "physics nonlinearity" hereafter. The PMT instrumentation and electronics may carry additional "instrumental nonlinearity", which is a nonlinear response between the created photons in the LS and the measured charge from the electronics. This nonlinearity is particularly non-trivial for the LPMTs. For a constant energy deposition, the LPMT charge response varies by up to 2 orders of magnitude depending on the position due to solid angle variations and optics. For example, a positron with 8 MeV kinetic energy produces up to 100 PE in the closest PMT, and on average 0.25 PE in the farthest one. In this context, the impact of instrumental nonlinearity is particularly delicate. Instead, the SPMT was designed to operate mainly in the single photon detection in the IBD energy range anywhere in the volume, so charge can be estimated either directly or via digital photon counting. Since both LPMT and SPMT are exposed to the common energy deposition, the SPMT acts as an independent digital and linear in-detector reference to the LPMT main system; i.e. enabling the dual calorimetry.

In addition to the energy nonlinearity, the photon collection in JUNO is strongly position dependent due to PMT solid angles, optical attenuations, reflections at material interfaces, shadowing due to opaque materials (e.g. SS connection bars), etc. The uncorrected instrumental nonlinearity can mimic an additional position non-uniformity, manifested most acutely closer to the detector edge where the LPMT charge response vary widely. The dual calorimetry based correction allows channel-wise nonlinearity control to reduce or disentangle such systematic response ambiguities. The residual position non-uniformity, now intrinsic due to the detector optics and mostly energy independent, has to be corrected as well to optimize the energy resolution.

The determination of MH imposes that the uncertainty of the positron kinetic energy scale should be better than 1%, and the effective energy resolution should be better than 3% [3, 8, 9]. These stringent requirements can only be achieved through a comprehensive calibration program. In this paper, we describe the calibration strategy for JUNO and demonstrate how the physics needs are satisfied. The remainder of the paper is organized as follows. In Sec. **2**, we discuss the approach of the energy scale calibration to combat the physics and instrumental nonlinearity. We then develop the method to minimize the energy resolution via correcting the position non-uniformity, in Sec. **3**. Based on these, we present the conceptual design of the calibration

hardware in Sec. **4**, and the calibration program that we envision in Sec. **5**, before concluding in Sec. **6**.

2 Energy scale calibration

A custom Geant4-based (version 9.4.p04) [10] software, called SNIPER [11], is used to perform calibration related simulations. SNIPER consists of the up-to-date JUNO detector geometries and optical parameters. The JUNO LS was tested in an decommissioned Daya Bay detector, so the LS optical parameters such as the light yield, absorption and re-emission probability were tuned to the data [12, 13]. The Rayleigh scattering length was measured in a separate bench experiment [14]. The optical parameters of the acrylic sphere, ultrapure water, and other materials were taken from bench measurements. The quantum efficiency and collection efficiency (angle-dependent) of the LPMT and SPMT were initially set at the average values from quality assurance tests, and can be adjusted individually in the simulation. The so-called "low energy" physics lists for the electron, positron and gamma are selected in SNIPER, based on the Daya Bay experience.

Table 1. List of radionuclides considered in the JUNO calibration system. For the ^{68}Ge source, it decays into ^{68}Ga via electron capture, then β^+-decay into ^{68}Zn. Although being a positron emitter, the kinetic energy of the positron will be absorbed by the enclosure, so only the annihilation gammas will be released.

Source	Type	Radiation
^{137}Cs	γ	0.662 MeV
^{54}Mn	γ	0.835 MeV
^{60}Co	γ	1.173 + 1.333 MeV
^{40}K	γ	1.461 MeV
^{68}Ge	e^+	annil 0.511 + 0.511 MeV
^{241}Am-Be	n, γ	neutron + 4.43 MeV
^{241}Am-^{13}C	n, γ	neutron + 6.13 MeV
(n,γ)p	γ	2.22 MeV
(n,γ)^{12}C	γ	4.94 MeV or 3.68 + 1.26 MeV

2.1 Calibration of physics nonlinearity

2.1.1 Selection of sources

For a large LS detector, thin-walled electron or positron sources would pose risk on leakage of radionuclides and difficulties on blockage of photons due to non-transparent materials (referred to as the shadowing effect hereafter). For simplicity, we consider γ sources ranging from a few hundred keV to a few MeV to cover the range of the prompt energy the IBDs. In addition, (α,n) sources ^{241}Am-Be (AmBe) and ^{241}Am-^{13}C (AmC) can be used to both provide high energy gammas, as well

as neutron capture signals on proton and carbon. The sources and types of radiations are listed in Table 1.

2.1.2 Model of physics nonlinearity

Most IBD positrons lose energy by depositing ionization energy (the same way as electrons) before they stop. A positron can either directly annihilate with an electron, or form either a para- or ortho-positronium bound state before it annihilates [15], producing either two or three gammas, respectively, with a total energy of 1.022 MeV. Therefore, the observed prompt energy of an IBD can be written as

$$E_{\text{prompt}} = E^e_{\text{vis}} + E^{\text{anni}}_{\text{vis}}. \qquad (2)$$

The first term describes the visible energy associated with the kinetic energy of the positron, which would be identical for an electron with the same energy, and the second term is the visible energy of the annihilation gammas. $E^{\text{anni}}_{\text{vis}}$ can be approximately calibrated using an enclosed ^{68}Ge source, although the IBD positron has sub-percent of probability of annihilating in flight, emitting higher energy gammas. Let us now define a physics nonlinearity

$$f_{\text{nonlin}} = \frac{E^e_{\text{vis}}}{E^e}, \qquad (3)$$

in which E^e is the true kinetic energy of an electron or positron. So if f_{nonlin} can be determined via calibration, then for each IBD event, the true kinetic energy of a positron can be reconstructed as

$$E^e = \frac{E_{\text{prompt}} - E^{\text{anni}}_{\text{vis}}}{f_{\text{nonlin}}}. \qquad (4)$$

A gamma converts its energy into the LS via secondary electrons. This internal connection allows a robust determination of f_{nonlin} using the gamma calibration data [16, 17]. Without loss of generality, let us model f_{nonlin} as a four parameter function, as used in the first Daya Bay spectral analysis [17],

$$f_{\text{nonlin}} = \frac{p_0 + p_3 E^e}{1 + p_1 e^{-p_2 E^e}}, \qquad (5)$$

where the exponential on the denominator enforces a decay of the physical nonlinearity at higher energy.

Let $P(E^e)$ denote the probability density function (PDF) of a given gamma source converting to secondary electrons/positrons via the Compton scattering, photoelectric effect, or pair production, at an energy E^e, determined from the simulation model. Then the visible energy of the gamma is simply

$$E^\gamma_{\text{vis}} = \int P(E^e) \times f_{\text{nonlin}}(E^e) \times E^e dE^e. \qquad (6)$$

Multiple sources in Table 1 lead to multiple Eqn. 6, so parameters in Eqn. 5 can be determined with redundancy.

The highest gamma energy point is 6.13 MeV (AmC), which is insufficient to cover the full energy range of IBD positrons. On the other hand, cosmogenic β background such as ^{12}B (Q value 13.4 MeV) is abundant in JUNO, about 1000 evts per day [3]. ^{12}B decays with a half life of 20 ms, which can be clearly identified by looking for delayed high energy β event (with a few percent mixture of ^{12}N, a β^+-emitter) after an energetic muon [18]. More than 98% of the ^{12}B β-decay into the ground state of ^{12}C, making it almost a pure β source. Therefore, despite its continuous spectrum, ^{12}B offers complementary constraints to $f_{\text{nonlin}}(E^e)$ at the high energy end. To combine the gamma source and ^{12}B data, we define a χ^2 as

$$\chi^2 = \sum_j^8 \left(\frac{M^\gamma_j - P^\gamma_j}{\sigma_j} \right)^2 + \sum_{i=0}^{100} \frac{(M^{\text{B12}}_i - P^{\text{B12}}_i)^2}{M^{\text{B12}}_i} \qquad (7)$$

where M^γ_j and P^γ_j are the measured and predicted visible energy peak of the jth gamma source, respectively, and σ_j is the corresponding uncertainty. The ^{12}B spectrum will be binned, and M^{B12}_i and P^{B12}_i are the number of measured and predicted events, normalized to the total measured events, in the ith visible energy bin.

2.1.3 Validation of calibration procedure

To validate this procedure, we use SNIPER to simulate bare gamma sources in Table 1 at the center, and ^{12}B decays uniformly distributed in the entire detector. The visible energy E_{vis} is estimated from the total PE by assuming a somewhat arbitrary scaling constant ($\sim$1345 PE/MeV) set by the 2.22 MeV gammas from the neutron-proton captures at the CD center. For each gamma source, the corresponding PDF $P(E^e)$ is extracted from the underlining Geant4 processes. For the^{12}B data, a cut of 5 MeV is applied to remove accidental background due to intrinsic ^{208}Tl in the liquid scintillator. In addition, a fiducial cut of a radius of less than 15 m is chosen to avoid energy leakage via Bremstralung close to the boundary. The data are also corrected for position non-uniformity using the procedure in later Sec. **3.1**. To obtain the predicted ^{12}B spectrum, the physics non-linearity (Eqn. 5) as well as a spectral smearing according to the energy resolution function (Eqn. 8) are applied in each iteration of the fit. The statistical uncertainty of each gamma peak is estimated to be better than 0.01% with 100,000 calibration events. The statistics of ^{12}B is assumed to be equivalent to one month running period, with approximately 70% fiducial acceptance.

(a) Gamma nonlinearity

(b) Boron Spectrum
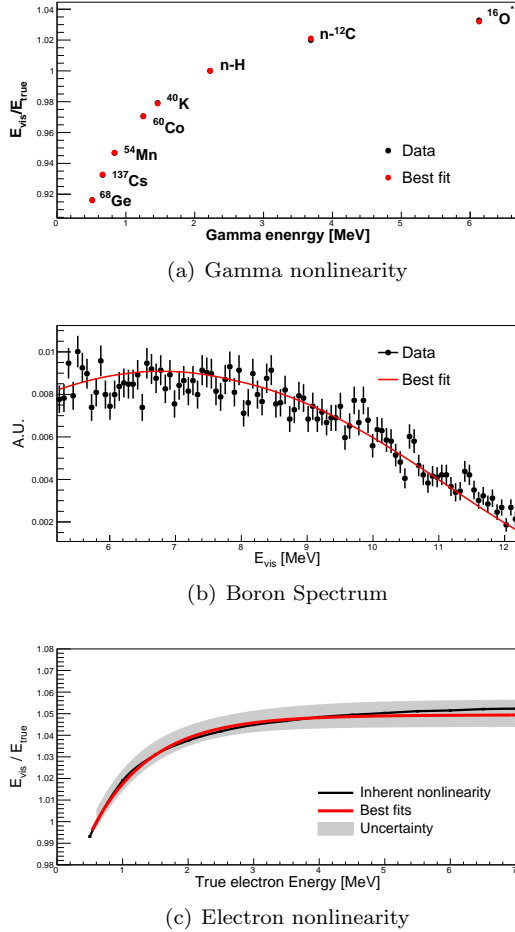

(c) Electron nonlinearity

Fig. 1. Fitted and simulated gamma nonlinearity(a), ^{12}B spectra (b), and electron nonlinearity (c). In all figures, black points (curve) represent the simulated data, and the red points (curves) are the best fits. Statistical uncertainties for the gamma sources are at a 0.01% level so are invisible from the figure. The 4.43 MeV gamma from the Am-Be neutron source is not used, as it is contaminated by the simultaneous nuclear recoil signals. In (b), the spectrum corresponds to roughly one month of ^{12}B data in the detector, and smearing due to energy resolution is included in the fit. In (c), the uncertainty band is evaluated using the procedure in Sec. 2.3.

With the above input, p_i is determined by Eqn. 6 using the χ^2 fit (Eqn. 7). For the gamma sources, the ratios of the best fit visible energy (Eqn. 6) to the true are compared to those from the simulated data in Fig. 1(a), where excellent agreement is found. For visual clarity, for sources with multiple gamma emissions, the horizontal axis is chosen to be the mean energy of the gammas. The best fit model for the ^{12}B visible spectrum is overlaid with simulated data in Fig. 1(b), where good

agreement is also observed. For comparison, we use the same SNIPER to produce the visible energy for individual mono-energetic electrons at the CD center and extract the true f_{nonlin}. Assuming no charge nonlinearity effects, the difference between best fit and the true electron nonlinearity is better than a 0.3% within the entire energy range, as shown in Fig. 1(c).

For a final sanity check, we perform SNIPER simulation on mono-energetic positrons at the CD center. The kinetic energy is reconstructed event-by-event using Eqn. 4, in which $E_{\mathrm{vis}}^{\mathrm{anni}}$ is obtained from the simulation of an enclosed ^{68}Ge source and f_{nonlin} is taken from the best gamma fit in the previous step. The residual bias in the reconstructed energy and the 1σ uncertainty band (see Sec. 2.3), as depicted in Fig. 2, is less than 0.6% over the entire range of the IBD energy, which is significantly better than the 1% requirement.
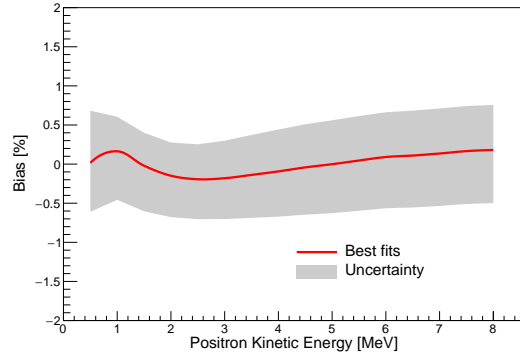

Fig. 2. Bias in the reconstructed positron kinetic energy as a function of true energy in the SNIPER simulation. The band represents the uncertainties in the calibration procedure, detailed in Sec. 2.3. The lowest kinetic energy in the figure is 0.5 MeV, to avoid artificial increase of the fractional bias when the kinetic energy approaches zero. The best fit does not center in the uncertainty band, as some systematic uncertainties are one-directional, e.g. the shadowing effect and energy loss effects.

2.2 Calibration of instrumental nonlinearity

The event-wise instrumental nonlinearity reflects the convolution of the channel-by-channel nonlinearity contributions. The nonlinearity fraction of each channel depends on the illumination, which depends on the location of the energy deposition. The best way to correct this is to calibrate each channel nonlinearity using a tuneable light source over the full illumination dynamic range: from a fraction of a PE up to around 100 PE per channel on average. To achieve a uniform illumination in all LPMTs with a linear intensity reference (SPMT), one should deployed the light source at the center of the CD with an intensity varying from 0.3 MeV (threshold) up

to 1.0 GeV equivalent. Such a system is demonstrated in Ref. [19], consisting of a ns-timing pulsed UV laser beam, directed into an optical fiber with a diffuser ball attached to its open end deployable along the central axis of the CD. The UV photon at 266 nm is foreseen to excite the LS thus enabling an output photon time profile similar to physics events. The combination of the dual calorimetry design and the deployable laser source is particularly powerful. The SPMT response is made linear in charge by design, therefore the total SPMT charge is an ideal in-detector light intensity reference, allowing a clean extraction of the LPMT channel-wise nonlinearity with varying laser intensity. This dual calorimetry metric cancels common effects between the LPMT and SPMT. Such a calibration scheme can yield remarkable performance, as illustrated in Fig. 3. Electron events from 1 to 8 MeV are uniformly simulated in the JUNO CD. We start with a very pessimistic LPMT response non-linearity (i.e. a channel-wise bias of 50% over 100 PE), which induces a seemingly energy dependent non-uniformity. For instance, if the non-uniformity obtained with 1 MeV energy deposition (Sec. **3**) is applied to correct the event-wise total charge of LPMT for all events, the mean bias in energy measurement in the fiducial volumn can still be as large as 2% at 8 MeV. For comparision, if the LPMT charge is calibrated channel-wise using the laser and SPMT, the event-wise residual instrumental non-linearity is reduced to ≤0.3%. Under more reasonable LPMT nonlinearity assumptions, the dual calorimetry laser calibration is expected to yield an event-wise linear instrumental response of better than 0.1%.
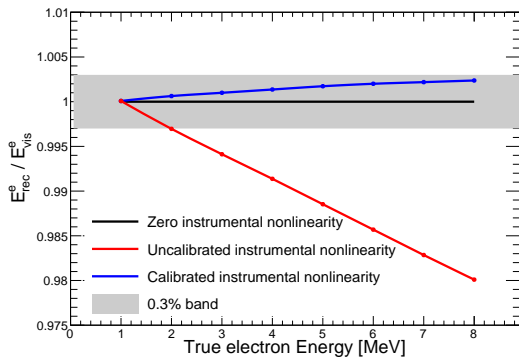

Fig. 3. Illustration of the impact of a large instrumental nonlinearity to the average energy scale of electrons (uniformly distributed in the detector) with and without channel-wise correction. The vertical axis is the ratio of the reconstructed energy based on measured charge from LPMT to the visible energy based on true charge of LPMT. The black line represents the perfect linear case. For the channel-wise instrumental nonlinearity for the LPMT, we assume that it grows linearly with the true charge, reaching 50% at 100 PE. Its impact

to the full volume event-wise energy scale, corrected for the position non-uniformity at 1 MeV, is shown as the red line. The same event-wise energy scale, corrected for the channel-wise non-linearity using the laser and dual calorimetry approach, is shown as the blue line. The grey band illustrates the residual uncertainty (0.3%) of this correction.

Any laser based nonlinearity calibration could suffer from residual biases arising from the time profile of optical photons, if the instrumental nonlinearity depends on the photon arrival time profile. The excitation time profile of laser may not be identical to that from the physical events, and even identical, the timing smearing due to for example Rayleigh scatterings is vertex dependent, not reflected by the center-only laser calibration. Such an effect can be well controlled by deploying a radioactive source and the UV laser to a same series of off-center positions.

Since the SPMT system is always monitoring the response of the detector with or without calibration sources, aside from the instrumental linearity, the SPMT offers unique insights on the detector uniformity and the stability of the LPMT response across the life-span of the experiment.

2.3 Evaluation of systematic uncertainties

The calibration methodology discussed above inevitably bares systematic uncertainties. We study these uncertainties, and evaluate the combined effects to the positron energy scale in this section.

2.3.1 Shadowing effect

A realistic source is not a point source. A typical source we envision in the calibration is shown in Fig. 4. The source is enclosed in a 6 mm by 6 mm cylindrical SS shell, covered by highly reflective Polytetrafluoroethylene (PTFE), and attached to a SS wire with 1 mm diameter. A PTFE connector about 20 cm above the source allows easy exchange of the source when desired. To maintain the tension in the wire, a weight covered with PTFE is also attached to the wire below the source, with a separation of about 20 cm. Despite the PTFE materials, optical photons can still be absorbed by these surfaces, leading to a small bias in visible energy.

To study this bias, a conservatively a 90% reflectivity is assumed for the PTFE surfaces. Only events with energy fully absorbed in the LS region are chosen from the simulation to decouple this effect with the energy loss in dead material (see next).
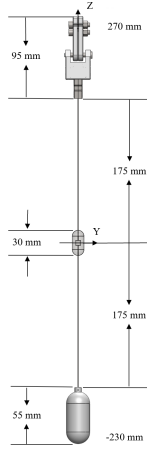
Fig. 4. Design of a typical source assembly. See text for details.

The resulting bias in comparison to the bare sources are shown in Fig. 5, which is less than 0.15% for all sources. The increase of the bias toward lower energy is expected due to the photon loss on the source shell, and the grow toward higher energy is due to more shadowing effect on the weight/connector.
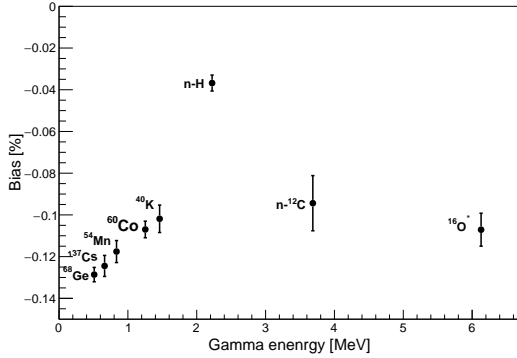

Fig. 5. Bias due to optical shadowing for individual gamma sources.

2.3.2 Energy loss effect

Some gamma energy can also deposit in the non-scintillating material, e.g. the enclosure of the source, leading to a leakage tail in the detected PE spectrum. The bias to the peak is referred to as the energy loss effect. As an example, the measured PE spectrum from the LPMTs for a realistic ^{60}Co source is shown in Fig. 6, in which contributions from the fully absorbed peak and the leakage tail are separately plotted.
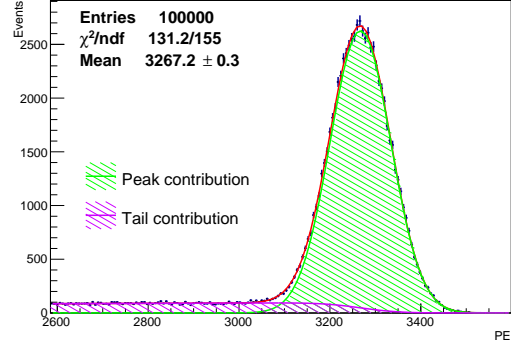

Fig. 6. The PE distribution of ^{60}Co source at the center of JUNO. Contributions from the fully absorbed events and energy loss tail are indicated in the figure. See Sec. 2.3.2 for details.

A fitting function with the energy loss effect taken into account [20] is adopted here to fit the simulated gamma spectra. The fractional difference of the best fit peak to those from the fully absorbed events are shown in Fig. 7, where residual biases are less than 0.1% for all sources.
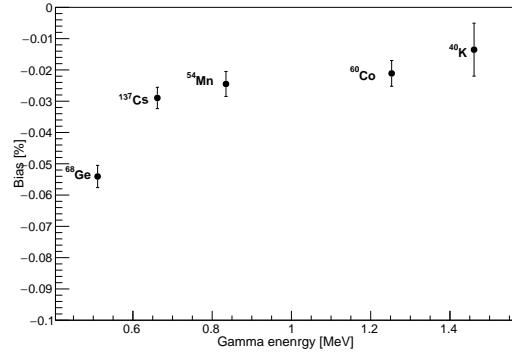

Fig. 7. Residual fit bias due to the energy loss effect for the gamma sources. Effects for higher energy gamma sources are negligible, so they are omitted from the figure.

2.3.3 PMT dark rate

Assuming an average dark rate of 30 kHz per LPMT channel, and a 350 ns readout time window, the dark rate pileup in any given physical event is estimated to be 189 PE. Such an offset in energy can be precisely calibrated using random triggers and subtracted. The contribution of this pileup to the energy resolution shall be discussed in Sec. **3**.

2.3.4 High energy gamma uncertainty

High energy gammas are essential to calibrate the electron nonlinearity at the high energy end. Such gammas can be produced via the (α, n) reaction when the daughter nucleus de-excites. For example, the ^{241}Am-^{13}C

source can produce a 6.13 MeV gamma, but mixed with some nuclear recoil energy. According to the SNIPER simulation, the positive bias caused by the nuclear recoil is at a 0.4% level. Although subtractable, this leads to a scale uncertainty at the high energy end.

2.3.5 Instrumental nonlinearity

As discussed in Sec. 2.2, the dual calorimetry technique in combination to the UV laser source in Ref. [19] and the radioactive sources is expected to provide a direct and clean measurement of the instrumental nonlinearity. The integral nonlinearity control is expected to be ≤0.3%, as shown in Fig.3, although 0.1% accuracy seems possible. This uncertainty is propagated as a fully correlated uncertainty in energy, but fully uncorrelated to the position dependent effect (next).

2.3.6 Position dependent effect

Since IBDs are detected throughout the detector, position dependent energy scale variation has to be corrected for. The impact of this correction on the energy resolution will be elaborated in Sec. **3**. As we will show

there, the mean scale bias after this correction is reduced to a 0.3% level, which is conservatively taken as a fully correlated uncertainty in energy.

2.3.7 Statistics

The statistical uncertainty of the gamma peak determination is driven by the number of calibration events. Based on fits as in Fig. 6, we validate that with 100,000 events, statistical uncertainties of all sources can be controlled to a 0.01% level, in agreement with the naive estimate.

2.3.8 Estimate of combined systematic uncertainty

The effects discussed above are summarized in Table 2. We assume that all the systematic can be corrected for, but with 100% uncertainty. We further separate the uncertainties either into correlated in different energy, or point-to-point (single point), depending on how they would drive individual energy points. For example, the uncertainties due to the shadowing effects are correlated among difference sources.

Table 2. A summary of the energy scale uncertainties.

source	correction	uncertainty	nature
shadowing effect	+0.1% - +0.2%	correction	correlated
energy loss effect	+0.05% - +0.1%	correction	correlated
high energy gamma uncertainty	−0.4%	correction	single point (6.13 MeV)
instrumental nonlinearity	n/a	(0.1,0.3]%	correlated
position dependent effect	−0.3%	correction	correlated
statistics	n/a	0.01%	point-to-point

To evaluate the combined effects, we produce toy data by randomly biasing the naked source values in Fig. 1(a) according to the 1σ uncertainties in Table 2, either in a correlated or point-to-point fashion. Except for the instrumental nonlinearity and the statistics in peak fitting, all uncertainties are equal to the absolute value of the correction. For each set of the toy data, a fit as in Sec. 2.1.2 is performed, yielding an electron nonlinearity curve. This is repeated many times. The 1σ distribution of these fitted models are overlaid in Figs. 1(c) and 2. The uncertainty band is more significant ($\sim 0.6\%$) across all energy, so the 1% JUNO requirement is safely satisfied.

3 Minimizing the energy resolution

Another key aspect of the calibration is to minimize the energy resolution for the IBD positron signals. In general, the fractional energy resolution for an average visible energy E_{vis} in MeV can be written as an approx-

imate formula

$$\frac{\sigma_{E_{\mathrm{vis}}}}{E_{\mathrm{vis}}} = \sqrt{\left(\frac{a}{\sqrt{E_{\mathrm{vis}}}}\right)^2 + b^2 + \left(\frac{c}{E_{\mathrm{vis}}}\right)^2}. \qquad (8)$$

The a term is the statistical term, which is mainly driven by the Poisson statistics of true PEs associated with E_{vis}. c term represents the contribution of a background noise term, i.e. the dark noise from the PMTs, which is always mixed with E_{vis} in the measurement. To set the scale, since the light yield for JUNO is approximately $Y_0 = 1345$ PE/MeV, a is about 2.7%. As mentioned in Sec. 2.3.3, dark rate induced energy bias is approximately $\Delta Q_{\mathrm{DR}} \sim 189$ PE, so c is estimated to be $\sqrt{\Delta Q_{\mathrm{DR}}/Y_0^2} = 1.0\%$. b is a constant term independent of the energy, and in the case of JUNO, dominated by the position non-uniformity. In Fig. 8, the average number of PE for the 511 keV gamma pairs vs. radius is shown for a few representative θ angle in spherical coordinate. Starting from the detector center, the gradual increase is a combined effect of due to variations in photon coverage and attenuation. The sharp decrease close to 15.5 m is due to the mismatch of the indices of refraction between

the acrylic and water - the closer the event to the edge, the more likely the total reflections and consequently the losses of photons. Within the same radius, there is an additional dispersion in θ due to geometrical and optical complications. The b term estimated from Fig. 10 is 6%, but can be largely removed with calibration.
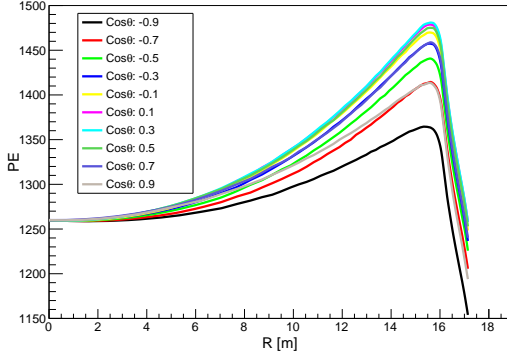

Fig. 8. Mean number of PEs for the 511 keV pairs as functions of radius, along a few representative polar angles (see legend).

The impact of the energy resolution (Eqn. 8) is studied in details in Ref. [3]. It was found, numerically, that the JUNO baseline requirement that the difference in the correct and wrong hierarchy fits of the neutrino energy spectrum reaches a $\Delta\chi^2 > 11$ in six years, could be translated into a convenient requirement on an equivalent resolution term $\tilde{a}$,

$$\tilde{a} \equiv \sqrt{(a)^2 + (1.6 \times b)^2 + \left(\frac{c}{1.6}\right)^2} \leqslant 3\%. \qquad (9)$$

Conceptually, the facts that the constant b term is not improving with detected energy, and that the contribution of the dark noise declines quickly with the energy, are reflected in factors 1.6 and 1/1.6, respectively. Note also that $\tilde{a}$ is only an effective parameter, and is not the detector energy resolution at 1 MeV.

3.1 Reducing b term: non-uniformity correction

Two complementary approaches can be used in characterizing the detector non-uniformity, a) to deploy radioactive sources in many locations in the detector, and b) to use uniformly distributed background events, e.g. spallation neutrons ($\sim$1.8 evt/s [3]). Although we focus on the first approach in this paper, it should be emphasized that the second approach would offer a powerful *in situ* cross check in the real experiment.

We define a non-uniformity function $g(r,\theta,\phi)$ as the light yield in a given position relative to that at the center. Ideally, to calibrate g, one would like to sample as many points, in particular in locations where it varies

quickly. Practically, however, our goal is to use finite calibration points to find a sufficiently good approximation. To study this, simulated data are produced using SNIPER with mono-energetic positrons from 0 to 8 MeV, uniformly distributed in the detector. Dark rate pileup is included as an independent Poisson-fluctuated offset with a mean value of 189 PE (Sec. 2.3.3). The visible energy in MeV for each event is estimated as

$$E_{\text{vis}} = (\text{PE}_{\text{tot}} - \Delta Q_{\text{DR}})/Y_0/g(r,\theta,\phi). \qquad (10)$$

In this study, $g(r,\theta,\phi)$ is systematically stepped down from the most complete knowledge to approximate models that we envision to obtain through calibration. After getting the resolution at each energy, (a, b, c) can be extracted and compare to the requirement in Eqn. 9.

3.1.1 Center IBDs

In this case, all positrons are produced at the center of the CD. Although the average light yield is slightly less in comparison to the full volume (Fig. 8), the position non-uniformity is completely absent. Interestingly, a fit using Eqn. 8 to the energy resolution yields a non-vanishing $b = 0.73\%$. $c = 1.38\%$ is also sizably larger than the naive dark rate estimate (1.0%). The origins of these non-Poisson fluctuations were traced in the simulation by switching off individual processes. The residual b is dominated by absorption and reemission of Cerenkov photon, leading to additional "constant" noise term in the detected PEs. The floor in c is due to fluctuations caused by the annihilation gammas, independent of the energy of the positrons.

3.1.2 Ideal non-uniformity correction

In the ideal case, uniformly distributed positrons are the calibration itself. The detector is divided into 20,000 equal-volume"pixels", and $g(r,\theta,\phi)$ is computed in each pixel for every energy, allowing a potential energy dependence (e.g. due to energy leakage at the edge).
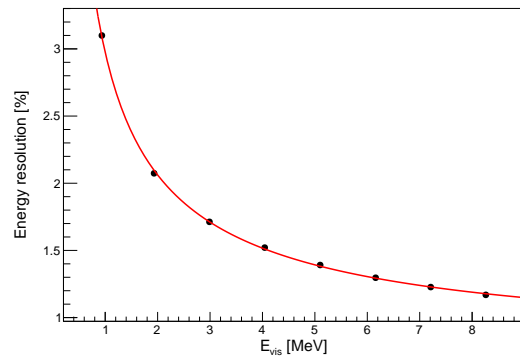

Fig. 9. Positron energy resolution vs. E_{vis} after the ideal non-uniformity correction.

The fit of the resolution is shown in Fig. 9, yielding a=2.57%, b=0.73%, c=1.25%, and $\tilde{a} = 2.93\%$ (Table 3).

The reductions in a and c terms, in comparison to those of the center IBDs, is due to the increase of full-volume light yield (Fig. 8). This scenario should serve as the most ideal reference for the calibration.

3.1.3 Utilizing azimuthal symmetry

The azimuthal symmetry in the JUNO detector allows the first simplification, that only g in a vertical half plane of the detector is needed. For illustration, $g(r,\theta)$ surface in the $\phi = 0$ plane for positrons with zero kinetic energy is shown in Fig. 10. The two-dimensional $g(r,\theta)$ function obtained at each positron energy is then applied to corresponding positron events. The resulting $\tilde{a}$ is 2.96%, a validity check of the azimuthal symmetry assumption.
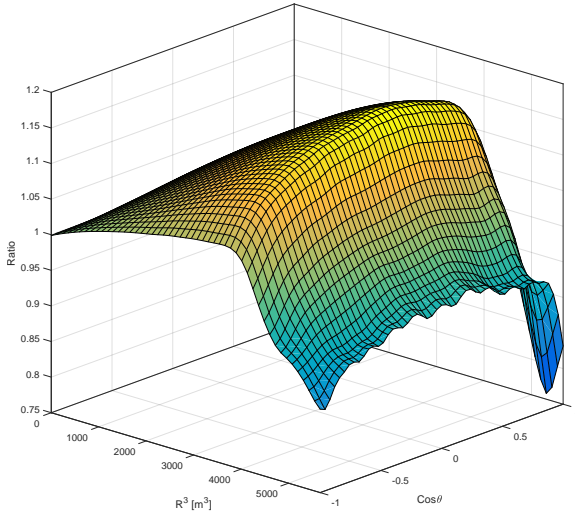

Fig. 10. The non-uniformity g in the $\phi = 0$ plane for 0 MeV positrons.

3.1.4 Single gamma source

One more step towards the reality is to use a single gamma line to replace $g(r,\theta)$ obtained by the hypothetical positron sources. We choose the 2.22 MeV neutron-proton capture gammas to allow direct comparisons to the spallation neutron capture signals in the real experiment, and to minimize the source shadowing effects (Fig. 5). After the application of this $g(r,\theta)$, $\tilde{a}$ is 2.98%. This also implies that the energy dependence of g can be safely omitted.

3.1.5 Finite calibration points

The next critical simplification is to select a list of "must-do" calibration points which would still give a satisfactory correction. Several pragmatic considerations are

- As observed in Fig. 10, there is no apparent symmetry in $g(r,\theta)$ that allows a vast simplification to the choice of points. However, the variation of g appears faster at the edge, which mandates more sampling points there.

- To constrain the surface of $g(r,\theta)$, the boundaries of the vertical half-plane are critical, i.e. the central axis of the detector and the inner circle at the LS-acrylic boundary. The central axis can be calibrated with good granularity, for example, one point every 2 meters for radius less than 12 m, one point every meter from 12 m to 17 m, and two points at 17.2 m and 17.5 m (27 points in total). For the acrylic boundary, the sphere is made up in 23 layers, each supported by SS fixtures with non-trivial impact to the optics. It would therefore be sensible to calibrate these 23 additional locations.

- For the region in between, if we start from the 23 points at the acrylic boundary and calibrate 9 more points along the radial line, this would make roughly 200 more points. Another practical consideration is the duration - if time spent at each calibration point (including source moving time) is 5 minutes, 200 points would take 16 hours, a reasonable duration.

- Realistically, not all points in (r,θ) are accessible. If we consider a SNO-like cable loop system [21] with anchors on the inner surface of the CD (see Fig. 12), some points too close to the vertical geometrical limits cannot be reached due to the loss of cable tensions (Ref. [22]). To allow a good coverage we consider two cable loops (Figs. 12 and 11) in the CD. Note that physically the two loops can be at different vertical planes, and azimuthal symmetry can be applied to combine them into a single (r,θ) half-plane.

Given the above, the optimization of calibration points is correlated with the choice of the two anchor locations (θ_1,θ_2) for the cable loops. An automatic optimization is performed using the following procedure. 1) We fix the 27+23 points along the two boundaries described above, and perform SNIPER simulations with 2.22 MeV gammas. 2) We go through all possible (θ_1,θ_2) combinations, each with its own accessible region in (r,θ) (Fig. 11). 3) For each (θ_1,θ_2), 200 points are randomly chosen, on which the 2.22 MeV simulations are made.

4) For each set of 200 (random) plus 50 (fixed) points, a smooth surface of $g(r,\theta)$ is constructed using a two-dimensional spline function. 5) Such $g(r,\theta)$ is applied to the uniform positron events, on which $\tilde{a}$ is extracted as a figure-of-merit. Steps 1) through 5) are repeated until a minimal $\tilde{a}$ is found. The final choice of the calibration points are illustrated in Fig. 11, in which the best anchor locations are $\theta_1 = 48°$ and $\theta_2 = 78°$. The resulting $\tilde{a}$ is 2.98%, very similar to that obtained using "infinite" calibration points.
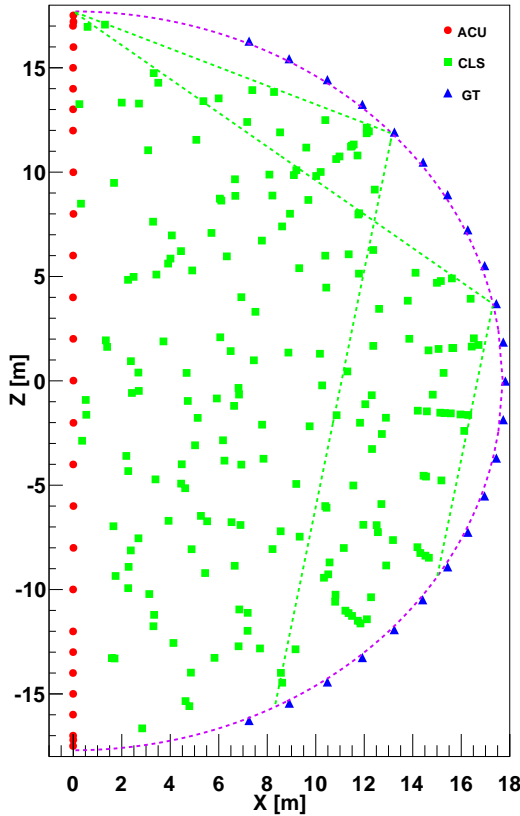

Fig. 11. Coverage of the 250 calibration points after optimization. The dashed lines are the upper and assumed outer (10° from vertical) boundaries of the coverage of the cable loops.

3.1.6 Vertex smearing

So far in making corrections to the reconstructed energy, we have used the true vertex in looking up $g(r,\theta)$. In reality, the event-by-event correction has to rely on the reconstructed vertex, which will in turn affects the quality of the correction. An algorithm based on time and charge information of LPMTs have been developed in Ref. [23] where a resolution of $8/\sqrt{E(\text{MeV})}$ cm (average distance between the true and reconstructed vertex)

was achieved. To study the impact to the overall resolution, we study three assumptions here, $8/\sqrt{E(\text{MeV})}$, $10/\sqrt{E(\text{MeV})}$, and $15/\sqrt{E(\text{MeV})}$ cm. For each simulated event, position smearing is made accordingly before applying $g(r,\theta)$ in Sec. 3.1.5. The corresponding $\tilde{a}$ is 3.01%, 3.05%, and 3.1%, respectively.

Another related effect is that we only know the calibration source location to certain precision, leading to a small smearing to $g(r,\theta)$. The hardware requirement is a precision of 3 cm [24] - significantly better than the reconstructed resolution at 1 MeV. It is verified that this contribution can be neglected.

3.1.7 LPMT quantum efficiency fluctuation

For each LPMT, the quantum efficiency (QE) was measured individually in the quality assurance process with an average value of $\sim$30% at 430 nm. The 1σ fractional variation of the QE was measured to be 7%. Therefore, instead of a constant, we assumed a random variation in QE of 7%, while keeping the average the same. The result is summarized in Table 3. Due to the PMT QE fluctuation, the $\tilde{a}$ deteriorates from 3.01% to 3.02%.

3.1.8 Realistic detector

So far we have discussed the simulation of an ideal JUNO with nominal parameters in SNIPER. A real detector can certainly differ from the simulation, so it is important to study whether an *in situ* calibration in a realistic detector can still achieve the required resolution. Five conservative alterations of the CD are considered:

1. The JUNO LPMT and readout electronics are designed to yield less than 1% dead channels ($\sim$180) in six years. We assume a CD with 1% LPMT failed in random positions.

2. Same as above but forcing an additional asymmetry among the bad channels (75:105, $\sim$1% culmulative binomial p value) in the two semispheres separated by the calibration plane (Fig. 11), breaking the assumed azimuthal symmetry.

3. The JUNO LS has been tested in one of the decommissioned Daya Bay detector for 1.5 years, so all optical parameters in JUNO LS are validated with this data. No temporal degradation of the light yield of this special detector has been observed with $\sim$0.5% standard deviation among measurements [13]. For conservativeness, we still assume that the light yield of JUNO Y_0 is reduced by 1% and 5% and study their effects.

4. A 4% reduction of the absorption length ($\sim$77 m at 430 nm [12] in SNIPER) can also produce a 1% reduction of Y_0. However, instead of a global reduction of light yield everywhere, the reduction of

absorption length alters the uniformity of the detector. We assume such scenario in the simulation.

5. The PMT resolution will also affect the energy resolution, if we naively use the measured charge (integral of the waveform) as the energy estimator. However, one should note that within the IBD energy range, most LPMTs are still working under the single photon counting regime, therefore one could use waveform-based photon counting analysis to avoid the resolution smearing. A successful application of this approach is in Ref. [25]. A waveform deconvolution technique [26] may also offer a better estimator for number of photons. Nevertheless, we assume a 30% single-photoelectron resolution for each LPMT to study the effect.

In each case, we recalibrate using the above program, obtain the $g(r,\theta)$ map, then apply it to uniformly distributed positrons. The results are summarized in Table 3. In the two cases where $\tilde{a}$ exceeds 3.1% (5% reduction of light yield, or the inclusion of 30% charge resolution for each PMT), sizable increase of the a term is observed (as expected), for which it is beyond the control of the calibration program. For all other cases, the impact of the residual $\tilde{a}$ is minor, indicating the effectiveness of the calibration program.

3.1.9 Bias in the energy scale

With the optimized 250 calibration points in Fig. 11, we also evaluate the residual bias in the energy scale. With nominal JUNO detector and the two-dimensional $g(r,\theta)$ above, the relative difference between E_{vis} (corrected using Eqn. 10) of uniform positron events to that at the CD center is less than 0.05%. For the five realistic detector conditions above, with the *in situ* calibration, the bias can be reduced to below 0.3% (adding the latter five effects in quadrature), as shown in Table 3. This residual bias has been included as a systematic uncertainty in the positron energy scale in Sec. 2.3.6.

3.2 Conclusion of the energy resolution

The step-by-step downgrade of the non-uniformity calibration from the ideal to the most realistic situation is summarized Table 3. One sees that the constant term b in the energy resolution can be minimized utilizing a single gamma source with about 250 points in a vertical half plane of the CD, bootstrapped to the entire CD using a smooth two-dimensional spline function in (r,θ). The nominal JUNO with the above calibration program will lead to an $\tilde{a}$ of 3.02%, in agreement with the requirement put forward in Ref. [3]. For other potential detector imperfections, although it is difficult to predict what may happen in a real detector, the individual impact can lead to a worst-case $\tilde{a}$ of 3.12%.

Table 3. Energy resolution after sequential downgrade from the ideal to realistic calibration. Values in parentheses indicate fitting uncertainties. For effects mentioned in Sec. 3.1.8, they are studied independently but by including all effects down to the PMT QE fluctuations.

Effects	a	b	c	$\tilde{a} = \sqrt{a^2 + (1.6b)^2 + (\frac{c}{1.6})^2}$	energy bias (%)
CD center	2.62(2)	0.73(1)	1.38(4)	2.99(1)	-
Ideal correction	2.57(2)	0.73(1)	1.25(4)	2.93(1)	-
Azimuthal symmetry	2.57(2)	0.78(1)	1.26(4)	2.96(1)	-
Single gamma source	2.57(2)	0.80(1)	1.24(4)	2.98(1)	-
Finite calibration points	2.57(2)	0.81(1)	1.23(4)	2.98(1)	-
Vertex smearing(8 cm)	2.60(2)	0.82(1)	1.27(4)	3.01(1)	-
PMT QE fluctuation	2.61(2)	0.82(1)	1.23(4)	3.02(1)	0.03(1)
1% PMT death (random)	2.62(2)	0.84(1)	1.23(5)	3.04(1)	0.09(1)
1% PMT death (asym)	2.63(2)	0.86(1)	1.20(4)	3.06(1)	0.23(1)
Y_0 reduced by 1%	2.62(2)	0.85(1)	1.25(4)	3.05(1)	0.09(1)
Y_0 reduced by 5%	2.68(2)	0.85(1)	1.28(5)	3.11(1)	0.09(1)
Absorption length reduced by 4%	2.62(2)	0.82(1)	1.27(4)	3.03(1)	0.07(1)
PMT charge resolution (30%)	2.72(2)	0.83(1)	1.23(5)	3.12(1)	0.08(1)

4 Conceptual design of the calibration system

The hardware design of the calibration system is mostly driven by the non-uniformity calibration requirements. As demonstrated in Sec. **3**, such a system should be capable to deliver a source along the central axis of the CD, the circle at the LS-acrylic boundary, and the region in between. The corresponding hardware design consists of several independent subsystems (Fig. 12), which will be discussed in turn.
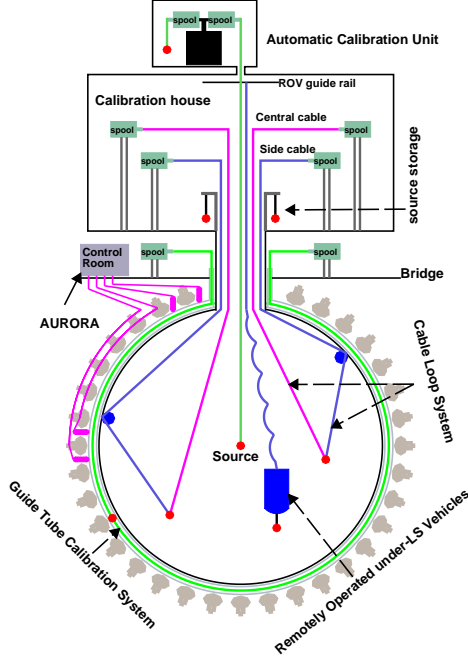
Fig. 12. Overview of the calibration system (not drawn to scale), including the ACU, two CLSs, the GT, and the ROV. The AURORA is a auxilliary laser diode system to monitor the attenuation and scattering length of the LS, which is beyond the scope of this paper.

4.1 Automatic calibration unit (ACU)

The ACU is developed to do calibration along the central axis of the CD. The design is very similar to the ACU in the Daya Bay experiment [27], with four independent spools mounted on a turntable. Each spool is capable to unwind and deliver the source under gravity through the central chimney of the CD, with a high positioning precision ($\sim$cm). Three sources can be deployed regularly, including a neutron source (AmC), a gamma source (^{40}K), and a pulsed UV laser source carried by an optical fiber with a diffuser ball attached to the end. To be flexible, the fourth spool will carry a replaceable source, for example a radioactive source or even a temperature sensor. Due to its simplicity and robustness, we envision to use it frequently during data taking to stabilize the energy scale, and to partially monitor the position non-uniformity.

4.2 Guide tube system (GT)

The GT is a tube looped outside of the acrylic sphere along a longitudinal circle. Within the tube, a radioactive source with cables attached to both ends gets driven

around with good positioning precision. The design of this system is discussed in details in Ref. [28]. Although physically outside of the CD, MeV-scale gammas can easily penetrate the 12 cm acrylic and deposit energy into the LS, despite that the full absorption peak is mixed with a somewhat significant leakage tail (correctable by fitting). Based on the simulation studies in Ref. [28], this subsystem is sufficient to calibrate the CD nonuniformity at the boundary.

4.3 Cable loop system (CLS)

As illustrated in Fig. 12, two CLSs lying in the two opposite half-planes serve the source deployment in off-axis positions. For each CLS, two cables are attached to the source, which also forms a loop to deliver and retract the source. The center cable goes upwards towards the chimney of the CD. The side cable winds through an anchor on the inner surface of the acrylic sphere, then towards the north pole of the CD, then vertically upwards through the chimney as well. By adjusting the lengths of the two cables, the source ideally could be delivered within an area bounded by the vertical lines through the anchor and the central axis. More realistic coverage measured by a CLS prototype will be reported in a separate paper [22]. Two CLSs with anchors at different polar angles allows a better coverage of the full half-plane, assuming an azimuthal symmetry. The overlapping points also allow direct checks on the azimuthal symmetry. In Sec. 3.1.5, the optimized polar angles of the two anchors have been determined to be 48° and 78°.

4.4 Remotely operated under-LS vehicles (ROV)

Locations other than the CLS plane could also turn out to be important, if there are significant local effects which break the azimuthal symmetry. These locations can be accessed by physical background events, for example, the spallation neutrons. Alternatively, we also plan to have a ROV similar to that in the SNO experiment [29], capable to deploy a radioactive source in the entire LS volume. Such a ROV needs to work with an independent positioning system. The mechanical design also needs to be optimized in size and surface reflection to minimize the loss of photons. Cleanliness control both in radioactive and chemical contaminations to the LS is another key design consideration. We envision that the ROV serves as a supplement of the ACU, CLS, and GT, and should be deployed very infrequently.

4.5 Positioning system

For the four subsystems above, ACU and GT have good positioning controls through accurate measurements of the cable lengths. For the CLS, due to friction in the loop and the self-weight of the cable, realistic

cables do not run in straight lines. Therefore, calculations based on naive trigonometric relations introduce significantly uncertainties in the source location [22]. For the ROV, it is even more complex as the positioning is needed during the navigation. For these purposes, an independent ultrasonic positioning system has been developed. Eight ultrasonic receivers will be mounted inside the acrylic sphere, and the source deployed by the CLS or ROV will carry a miniature ultrasonic emitter [30]. Based on the prototype tests, such a system is capable to provide a positioning precision to better than a few cm.

5 JUNO calibration program

Based on all discussions above, we can now streamline the calibration program. The rates of the radioactive source are set to be around 100 neutron or gamma emissions per second (except ^{40}K which can only be made with natural potassium salt), so that the data rate during the calibration does not differ too much from that during the neutrino data taking ($\sim$1000 Hz). Under this rate, a one-minute calibration run can achieve a better-than 0.1% statistical uncertainty to the gamma peaks.

Similar to the Daya Bay calibration, we envision to separate the routine calibration into two potential frequencies, weekly and monthly. As a requirement, such deployment should not introduce noticeable radioimpurity into the detector such as Radon. We also plan to have infrequent but comprehensive special calibrations. The nominal speed of the source movement is about 1 m/min. Due to the size of the detector, the source moving time should also be considered.

5.1 Weekly calibration

The weekly calibration is designed to track the major change of the detector such as the variations in the light yield of the LS, PMT gains, and electronics. As shown in Table 4, the neutron source (AmC) will be deployed to five locations along the central axis. The UV laser diffuser ball will be deployed to the CD center and pulsed with a repetition rate of 50 Hz under ten different intensities (equivalent energy from 0.3 MeV to 1 GeV), to allow channel-wise instrumental calibration using the dual calorimetry. Each laser run will have a duration of 2 minutes to allow a similar statistics as the radioactive sources.

5.2 Monthly calibration

The monthly calibration goes through a limited key points in Fig. 11, given that a priori a more elaborated calibration has been performed (see below), and that the temporal change of the detector is minimal. As shown in Table 5, the ACU, CLS, and GT will all be operated during the calibration. The UV laser will also be deployed to a same off-center location as the AmC to allow the study of time-profile dependence of the charge measurement (Sec. 2.2). To balance the extensiveness and time cost, we select the full sets of 27 and 23 points from the ACU and GT, and about 40 typical points in CLS to monitor the non-uniformity of the CD.

5.3 Special calibration

A special calibration is likely to be carried out at the early stage of the experiment to achieve a basic understanding of the CD performance, and then a few times throughout the JUNO live time. Multiple sources will be deployed to the CD center to study the nonlinearity. In addition, the AmC neutron source will be deployed to the full set of 250 points (Fig. 11) using the ACU, CLS and GT. As a baseline, we envision not to use the ROV at the beginning of the experiment due to purity concerns, but may relax this in the future. An estimate time cost for a special calibration is shown in Table 6.

Table 4. Weekly calibration

Source	Energy [MeV]	Points	Travel time [min]	Date taking time [min]	Total time [min]
Neutron (Am-C)	2.22	5	58	5	63
Laser	/	10	58	20	78
Total	/	/	116	25	141 ($\sim$2.4 h)

Table 5. Monthly calibration

System	Source	Points	Travel time [min]	Date taking time [min]	total time [min]
ACU	Neutron (Am-C)	27	93	27	120
ACU	Laser	27	93	54	147
CLS	Neutron (Am-C)	40	293	40	333
GT	Neutron (Am-C)	23	50	23	73
Total	/	/	529	144	673 ($\sim$11.2 h)

Table 6.   Special calibration

Source	Energy [MeV]	Points	Travel time [min]	Date taking time [min]	total time [min]
Neutron (Am-C)	2.22	250	680	1250	1930
Neutron (Am-Be)	4.4	1	58	15	73
Laser	/	8	58	16	74
^{68}Ge	0.511×2	1	58	15	73
^{137}Cs	0.662	1	58	15	73
^{54}Mn	0.835	1	58	15	73
^{60}Co	1.17+1.33	1	58	15	73
^{40}K	1.461	1	58	100	158
Total	/	/	1086	1441	2527 ($\sim$ 42 h)

6   Summary

We have carried out a comprehensive study to develop a multi-faceted calibration strategy for JUNO to secure its full potential to determine the neutrino mass hierarchy. This study is based on the most up-to-date JUNO simulation software, including all major features in the detector design. We demonstrate that using various gamma and neutron sources, in combination with a pulsed UV laser with precise intensity monitoring, we can determine the nonlinear energy scale of the positrons to a sub-percent level within the entire energy range of the IBDs. This is made particularly robust by the dual calorimetry of independent LPMTs and SPMTs, allowing a clean determination of instrumental nonlinearity. We also develop a multi-positional source deployment strategy, and verify that with a selection of 250 key positions in a vertical plane of the detector and by utilizing the azimuthal symmetry, we can control the non-stocastic fluctuations and achieve an effective energy resolution $\tilde{a}$ of 3.02% with the nominal JUNO detector parameters, satisfying the physics needs. This calibration plan requires a multi-component source deployment hardware including a vertical spooling system covering the central axis of the CD, a guide tube system attached to the acrylic sphere, two cable loops to cover a large fraction in a vertical plane, and a supplementary "4π" coverage "submarine". In the end, we separate the calibration tasks into different frequency categories to ensure both the timeliness and the comprehensiveness. We demonstrate that with such a calibrate strategy, the challenging requirements on the neutrino spectrum measurement of JUNO can be achieved with redundancy.

References

1 M. Tanabashi et al. (Particle Data Group), Phys. Rev. D 98, 030001 (2018)

2 R. D. McKeown, P. Vogel, Physics Reports 394 315-356 (2004)

3 Fengpeng An et al, Phys. G: Nucl. Part. Phys. 43 030401 (2016)

4 S. T. Petcov and M. Piai, Phys. Lett. B 533, 94 (2002)

5 S. Choubey, S. T. Petcov and M. Piai, Phys. Rev. D 68, 113006 (2003)

6 J. Learned, S. Dye, S. Pakvasa and R. Svoboda, Phys. Rev. D 78, 071302 (2008)

7 L. Zhan, Y. Wang, J. Cao and L. Wen, Phys. Rev. D 78, 111103 (2008)

8 L. Zhan, Y. Wang, J. Cao and L. Wen, Phys. Rev. D 79, 073007 (2009)

9 Li Y F, Cao J, Wang Y and Zhan L, Phys. Rev. D 88 013008 (2013)

10 Agostinelli S et al. (GEANT4), Nucl. Instrum. Meth. A506 250-303 (2003)

11 Lin, Tao et al., J.Phys.Conf.Ser. 898 no.4, 042029, arXiv:1702.05275 (2017)

12 Y. Zhang, Z.Y. Yu, X.Y. Li et al., Nucl. Instrum. Meth. A967, 163860 (2020)

13 Z.Y. Yu at al. "Optimization of the JUNO liquid scintillator composition using a Daya Bay anti-neutrino detector", JUNO Doc-DB-5860 (2020)

14 Zhou X, Liu Q, Wurm M, et al., Rev Sci Instrum. 86(7) 073310 (2015)

15 D. Franco, G. Consolati and D. Trezzi, Phys. Rev. C 83, 015504 (2011)

16 J. Detwiler Ph. D. thesis, Standford University (2005)

17 F. P. An et al., Phys. Rev. Lett. 112, 061801 (2014)

18 S. Abe et al. (KamLAND Collaboration) Phys. Rev. C 81, 025807 (2010)

19 Y. Zhang et al., JINST 14 P01009 (2019)

20 Jia-Hua Cheng et al., arXiv 1603.04433 (2016)

21 J. Boger et al., Nucl. Instrum. Meth. A 449, 172-207 (2000)

22 Y. Zhang et al., manuscript in preparation

23 Q. Liu et al., JINST 13 T09005 (2018)

24 Zelimir Djurcic et al., arXiv:1508.07166 (2015)

25 D. S. Akerib et al. (LUX Collaboration),Phys. Rev. D 101, 042001 (2020)

26 Yongbo Huang et al., Nucl. Instrum. Meth. A895, 48-55 (2018)

27 J. Liu et al., Nucl. Instrum. Meth. A750, 19 (2014)

28 Yuhang Guo et al., JINST 14 T09005 (2019)

29 J. F. Amsbaugh et al., Nucl. Instrum. Meth. A579, 2054 (2007)

30 Zhu, G., Liu, J., Wang, Q. et al., NUCL SCI TECH 30, 5 (2019)